Radome diagnostics - source reconstruction of phase objects with an equivalent currents approach

Persson, Kristin; Gustafsson, Mats; Kristensson, Gerhard; Widenberg, Björn

2012

Total number of authors:
4

Radome diagnostics — source reconstruction of phase objects with an equivalent currents approach

Kristin Persson, Mats Gustafsson, Gerhard Kristensson, and Björn Widenberg

Kristin Persson, Mats Gustafsson, and Gerhard Kristensson
{Kristin.Persson,Mats.Gustafsson,Gerhard.Kristensson}@eit.lth.se

Department of Electrical and Information Technology
Electromagnetic Theory
Lund University
P.O. Box 118
SE-221 00 Lund
Sweden

Björn Widenberg
bjorn.widenberg@gknaerospace.com

Radomes & Antennas
GKN Aerospace Applied Composites
P.O Box 13070
SE-580 13 Linköping
Sweden

Abstract

Radome diagnostics are acquired in the design process, the delivery control, and in performance verification of repaired and newly developed radomes. A measured near or far field may indicate deviations, *e.g.*, increased side-lobe levels, but the origin of the flaws are not revealed. In this paper, radome diagnostics are performed by visualizing the equivalent surface currents on the 3D-radome body, illuminated from the inside. Three different far-field measurement series at $10\,\text{GHz}$ are employed. The measured far field is related to the equivalent surface currents on the radome surface by using a surface integral representation. In addition, a surface integral equation is employed to ensure that the sources are located inside the radome. Phase shifts, insertion phase delays (IPD), caused by patches of dielectric tape attached to the radome surface, are localized. Specifically, patches of various edge sizes $(0.5 - 2.0\,\text{wavelengths})$, and with the smallest thickness corresponding to a phase shift of a couple of degrees are imaged.

1 Introduction and background

A radome encloses an antenna to protect it from *e.g.*, environmental influences. Depending on the properties of the shielding antenna and the environment in which it operates, the radome has different appearance and qualities. The radome is ideally electrically transparent, but in reality, radomes often reduce gain and introduces higher side-lobe levels, especially flash (image) lobes caused by reflections on the inside of the radome wall and reflections within the wall appear [6, 20]. Moreover, the electromagnetic wave radiated by the antenna changes its direction when passing through the radome, and, if not compensated for, boresight errors occur [6, 20].

New radomes must fulfill specified tolerance levels, and repaired radomes must be checked according to international standard and manufacturers maintenance manuals [20]. Consequently, there is a demand for diagnostic tools verifying the electrical properties of the radome. The verification test is often performed with a far-field analysis. Due to the radome, a measured far field may indicate boresight errors, amplitude reductions, introduction of flash (image) lobes, and increased side-lobe levels. However, it is not feasible to determine the cause of the alteration, *i.e.*, the location of defect areas on the radome, from the far-field data alone. Further investigations are often required, *e.g.*, cracks can be localized by employing ultrasonics [31]. Moreover, the phase alteration caused by the radome, *i.e.*, the insertion phase delay (IPD) on the surface of the radome, is commonly investigated to localize deviations. One way to measure the IPD is with two horn antennas aligned at the Brewster angle [29].

An alternative diagnostic method is presented in this paper, where the tangential electromagnetic fields — the equivalent surface currents — on the outside of the radome surface are reconstructed from a measured far field. The reconstruction is performed on a fictitious surface in free space, located precisely outside the physical surface of the radome, *i.e.*, no *a priori* information on the material of the radome is assumed. Both amplitude and phase are investigated. The effect of metallic

defects attached to a radome has previously been investigated in [26–28]. In this paper, we focus on imaging the phase changes introduced by a monolithic (solid) radome and patches of dielectric tape attached to its surface. These phase changes are interpreted as the IPD.

Three different far-field measurement series (at 10 GHz) are employed. In each series, both polarizations are collected over a hemisphere. Moreover, for each series, three different configurations are investigated; (0) antenna, (1) antenna together with the radome and (2) antenna together with the radome where patches of metal or dielectric material are attached to the surface. To clarify, different defects are applied to the radome in conf. (2) in the different series; defects consisting of copper plates (first series), squares of dielectric tape (second series), and the letters LU of dielectric tape (third series). The results of the first measurement series (metal defects) are employed to set the regularization parameters used in the subsequent series. In the two last measurement series, patches of dielectric tape, which mainly effect the phase of the field, are attached to the radome. The sizes of the patches vary, with a smallest dimension of 0.5 wavelengths. The dielectric patches model deviations in the electrical thickness of the radome wall, and the results can be utilized to produce a trimming mask for the illuminating areas. A trimming mask is a map of the surface with instructions of how the surface should be altered to obtain the desired properties, *e.g.*, a smooth IPD or low side- and flash-lobe levels. Diagnosis of the IPD on the radome surface is also significant in the delivery control to guarantee manufacturing tolerance of radomes.

The method to reconstruct the equivalent surface currents is based on a surface integral representation combined with an electric field integral equation (EFIE). The set-up is axially symmetric and a body of revolution method of moments (MoM) code is employed, with special attention taken to the calculation of the Green's function [13]. Regularization is performed by a singular value decomposition (SVD).

Prior radome diagnostics of spherical radomes utilizing a spherical wave expansion (SWE), applicable to spherical objects, are given in *e.g.*, [12], where the IPD and defects in the radome wall are investigated. Moreover, an early attempt to employ the inverse Fourier transform in radome diagnostics, is reported in [11].

The interest in surface integral representations as a tool in diagnostics has increased rapidly over the last years where different combinations and formulations based on a surface integral representation, the electric (EFIE) and magnetic (MFIE) field integral equations are utilized [1, 4]. Specifically, the influences of metallic defects attached to a radome are diagnosed in [26–28]. In [3] an iterative conjugate-gradient solver is utilized to find and exclude radiation contributions from leaky cables and support structures and in [10] antennas are characterized. Defect elements on a satellite antenna and a circular array antenna are localized in [18, 19], where a MoM code with higher order basis functions are implemented together with a Tikhonov regularization. Higher order basis functions and multilevel fast multipoles are utilized in [9] to recreate equivalent surface currents on a base station antenna from probe corrected near-field measurements. A surface integral representation is applied in [22, 23] to diagnose antennas. Furthermore, in [22] a conjugate-gradient solver and a singular value decomposition are shown to give similar results.
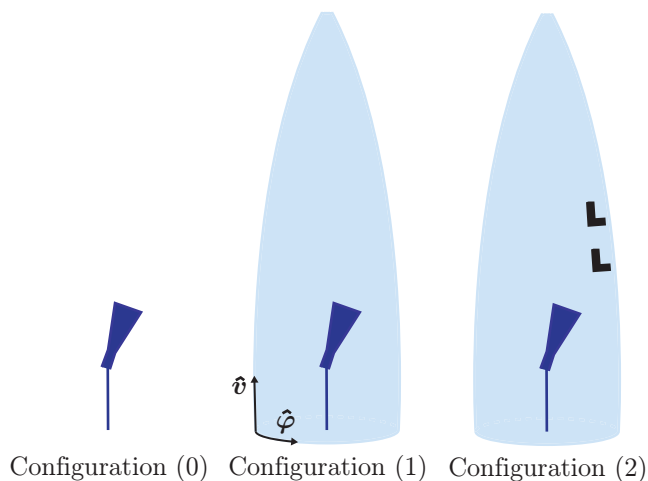
Configuration (0) Configuration (1) Configuration (2)

Figure 1: Description and notation of the configurations referred to throughout the paper. The middle figure shows the unit vectors of the coordinate system in which the reconstructed fields are expressed.

The focus of this paper is radome diagnostics, *i.e.*, to localize patches of dielectric tape attached to its surface from measured far-field data. In Section 2.1, the set-up, the compact test range, and the measured far field are described. The IPD and different visualization options — the electric or the magnetic field — are discussed in Section 2.2. In Section 3, an outline of the reconstructing algorithm is given. Imaging results are viewed and analyzed in Section 4, whereas conclusions and discussions of future possibilities are finally given in Section 5.

2   Radome diagnostics

A measured far field of an antenna and radome configuration may indicate unwanted deviations; *e.g.*, increased and changed side lobes, and boresight errors. To find the origin of the errors, diagnostic tools are essential. Here, far-field measurements from a compact test range is utilized to localize phase shifts, insertion phase delays (IPD) on the radome surface, caused by the radome and attached patches of dielectric tape.

2.1   Measurement data and set-up

Three different measurement series are conducted at $10\,\mathrm{GHz}$. Each measurement series consists of three configurations; antenna — conf. (0), antenna together with the radome — conf. (1), and antenna together with the radome where defects are attached to the surface — conf. (2), see Figure 1. Different defects are applied to the radome in conf. (2) in the different series; defects consisting of copper plates (first series), squares of dielectric tape (second series), and the letters LU of dielectric tape (third series). To clarify, conf. (0) and (1) are the same in all three series.
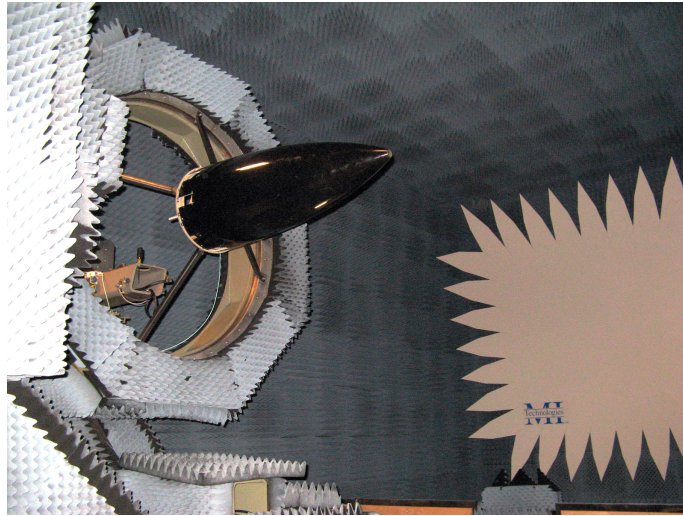
Figure 2: Photo of the measurement set-up in the compact test range.

The reason for doing these all over is that the measurement series were obtained at different times. In this way, we avoid the influence of small deviations in the mechanical and electrical set-up together with relative phase and amplitude shifts between the series. The configuration number is indicated as a superscript on the fields, whereas the field component is showed by a subscript, *i.e.*, $H_{\mathrm{v}}^{(0)} = \hat{\boldsymbol{v}} \cdot \boldsymbol{H}^{(0)}$ is the magnetic component directed along the height of the radome surface when only the antenna is present (*cf.*, notation in Figure 1).

The far-field measurements were carried out at a compact test range at GKN Aerospace Applied Composites, Linköping, Sweden, see Figure 2 [33]. The far field is measured on a hemisphere by turning the radome between $0° - 90°$ in the polar plane (described by θ) for each azimuthal turn (described by φ), where θ and φ are standard spherical coordinates, see Figure 3 for definitions and notational system. Measurements in the polar plane are continuously recorded at $1°/\mathrm{s}$, whereas the measurements along the azimuthal plane are discrete and thereby more time consuming. The field is sampled every second degree in the azimuthal plane and every degree in the polar plane. A reduction of the sample density by a factor of two in the polar plane is not noticeable in the imaging results, indicating that the sample densities are satisfactory [14, 34]. Measuring one configuration, both polarizations, took approximately nine hours.

The measured far field for both the co- and cross-polarization and the three different configurations is given in Figure 4, for measurement series number three. The figure shows a cross section in the polar plane of the fields through the main lobe, and it is observed that the radome — conf. (1) — changes the far field. Attaching patches of dielectric tape in the form of the letters LU to the radome surface — conf. (2) — alters the field a little more, which is hardly visible in the figure. Moreover, the origin of the defects can hardly be determined from the far-field data alone. The far fields of the other two measurement series have similar appearance.

In the far-field measurements no probe compensation is necessary [34]. Moreover,
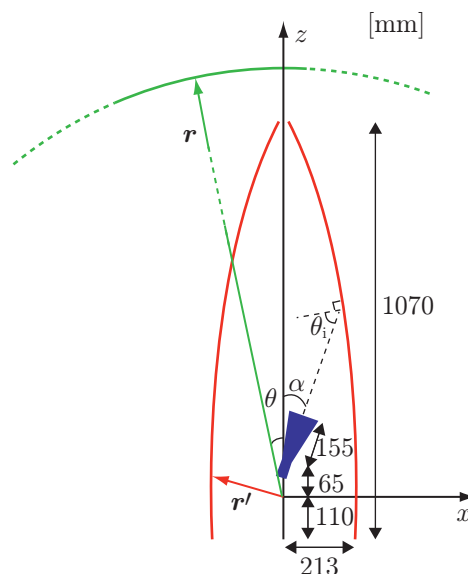
Figure 3: The geometry of the antenna, radome and far-field hemisphere. The center of rotation is located at the origin. The dominating polarization of the electric field on the antenna aperture is directed along the y-axis. The incline of the antenna is $\alpha = 22.3°$. An approximation of the incident angle is given by $\theta_i \approx 60°$. The far field is described in a spherical coordinate system with the polar angle θ.

in a compact range, where the radome and antenna is moved instead of the transmitting feed antenna, the off-set between the aperture of the antenna and the center of rotation causes a negligible amplitude change and a small phase shift during the measurement rotations. This can be corrected by probe compensation where the antenna aperture is mathematically translated to the center of rotation [14]. However, we have no interest in the absolute phase, only the phase difference between measurement configurations. This means that, as long as the set-up is rotated in the same way during all measurements, the off-set causes no problem. The far-field radius, r in Figure 3, is set to 1800 m. Larger radii give only negligible differences in the results.

The antenna is a pyramidal X-band horn antenna. The square aperture is $8 \times 8\,\mathrm{cm}^2$. The antenna is mounted at an angle $\alpha = 22.3°$, and it has a dominating electric field component in the y-direction, see Figure 3. The feed in the chamber is a linearly polarized standard X-band feed. The feed is turned 90° in order to measure both polarizations.

The radome is monolithic (solid) and covered with a thin layer of varnish. The dielectric material of the bulk has a relative permittivity of 4.32 and a loss tangent of 0.0144. The varnish has a, to us unknown, higher relative permittivity. The thickness of the radome wall varies between $7.6 - 8.2\,\mathrm{mm}$. The geometry is shown in Figure 3, and the height of the radome corresponds to 36 wavelengths at 10 GHz. In the investigations, patches of dielectric tape (Scotch Glass Cloth Electrical Tape 69-1") are attached to the radome. Waveguide measurements of the relative permittivity of the tape at Saab Dynamics, Linköping, Sweden, gave a value of $\epsilon_r \approx 4.1$
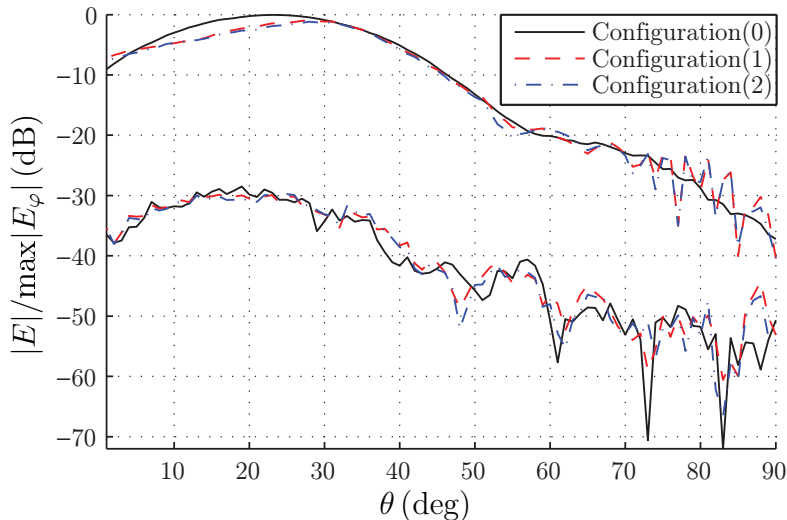
Figure 4: Co- and cross-polarization of the measured far field at $10.0\,\text{GHz}$ through the main lobe ($\varphi = 0$). The top three lines correspond to the three different configurations of the co-polarization, $E = E_\varphi$, and the three lower ones to the cross-polarization, $E = E_\theta$, respectively. In conf. (2) the radome has dielectric letters LU attached to its surface, see Figure 1. All values are normalized to the maximum value of the co-polarization when only the antenna is present (conf. (0)).

assuming the thickness of one layer to be approximately $0.15\,\text{mm}$. The losses of the tape are assumed negligible.

2.2 IPD and visualization options

In performance evaluations of radomes, the phase shift of the electromagnetic field, due to the passage through the radome wall, is important. This quantity is called the electrical thickness of the radome or the insertion phase delay (IPD), and it relates the phase shift in the radome wall to the phase shift in free space [6]. For a plane wave applies

$$\text{IPD} = \angle T - \frac{\omega}{c_0} d \cos \theta_\text{i} \tag{2.1}$$

where T is the complex transmission coefficient, which depends on the incidence angle, the parameters of the radome wall, and the polarization of the electromagnetic field [6]. The last term of (2.1) removes the phase shift of free space, where ω is the angular frequency, c_0 is the speed of light in free space, d is the thickness of the radome wall, and θ_i is the incident angle of the plane wave. In this paper, we consider reconstructed phase differences to visualize the IPD. In Section 4, the phase change of one field component, due to the radome, the defects, or both, is imaged.

The phase change, due to the attached dielectric patches, is reconstructed in Section 4. To verify the results, an approximate value of the phase change, due to one layer tape, is calculated. Thus, under the assumption of negligible reflections
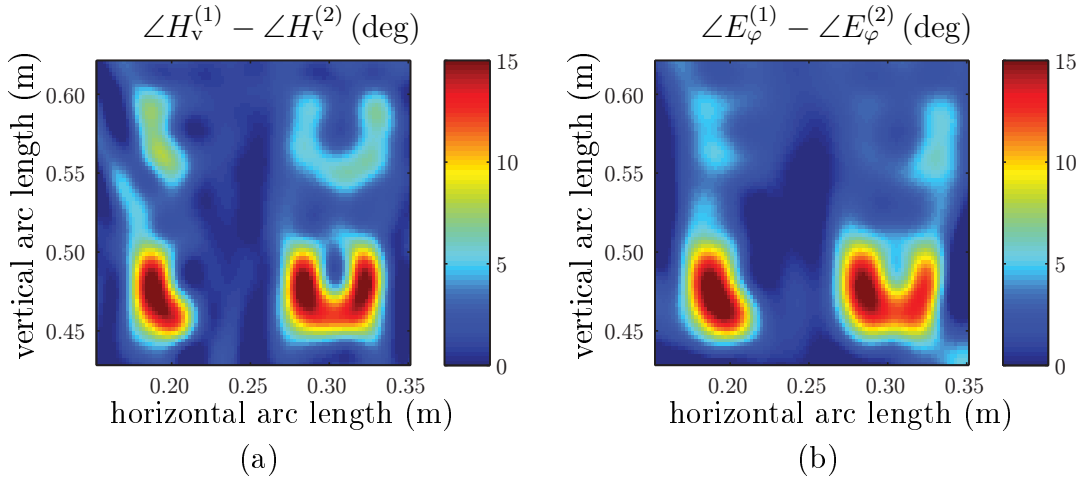
Figure 5: The reconstructed phase differences between conf. (1) and conf. (2). In conf. (2), dielectric patches in form of the letters LU are attached to the surface. The horizontal arc length corresponds to the center value of the height viewed on the y-axis, and this definition is utilized throughout the paper. a) The magnetic component H_{v}. b) The electric component E_{φ}.

and a homogeneous dielectric patch, the IPD can be expressed as [6]

$$\mathrm{IPD} = \frac{\omega}{c_0}\left\{\mathrm{Re}\,\sqrt{\epsilon_{\mathrm{r}}(1-\mathrm{j}\tan\delta)}\cos\theta_{\mathrm{t}} - \cos\theta_{\mathrm{i}}\right\}d_{\mathrm{p}} \tag{2.2}$$

for both polarizations. The relative permittivity of the tape is $\epsilon_{\mathrm{r}} \approx 4.1$, the loss tangent ($\tan\delta$) is negligible, the thickness of one layer tape is $d_{\mathrm{p}} \approx 0.15\,\mathrm{mm}$, and the transmission angle of the field is denoted θ_{t}. Assuming the incident angle to be in the interval $[40°, 80°]$, see Figure 3, gives an approximate phase shift of $2° - 3°$, per layer.

For large homogeneous slabs, the phase difference is the same for both the electric and the magnetic fields. However, a difference occurs when small patches of dielectric material are attached to the surface of the radome. In our investigations we conclude that the magnetic field gives the best image of phase defects, see Figure 5. As a consequence, this component is the one imaged in Section 4. In Figure 5a, the phase change, due to the dielectric letters LU, is visualized for the magnetic field component H_{v}, whereas the same phase difference is showed in Figure 5b for the electric field component E_{φ}. A qualified explanation of this difference is obtained by considering the induced current $\boldsymbol{J}_{\chi_{\mathrm{e}}} = \mathrm{j}\epsilon_0\chi_{\mathrm{e}}\omega\boldsymbol{E}^{(2)}$, see Appendix A for details. If the induced current is of electric nature, the electric field dominates in the near-field region, whereas the magnetic field is smoother [16]. A plausible assumption is that the induced charges in the dielectric give rise to dominating irrotational currents (electric charges) instead of solenoidal currents (loop currents). Hence, it is conjectured that this extra contribution to the electric near field, due to the defects, makes the defects appear less clear.

To further investigate the near fields, we have simulated the transmission using the software CST Microwave Studio, see Figure 6. An electric field polarized in the x-direction, propagating along the z-axis, illuminates the dielectric letter L located
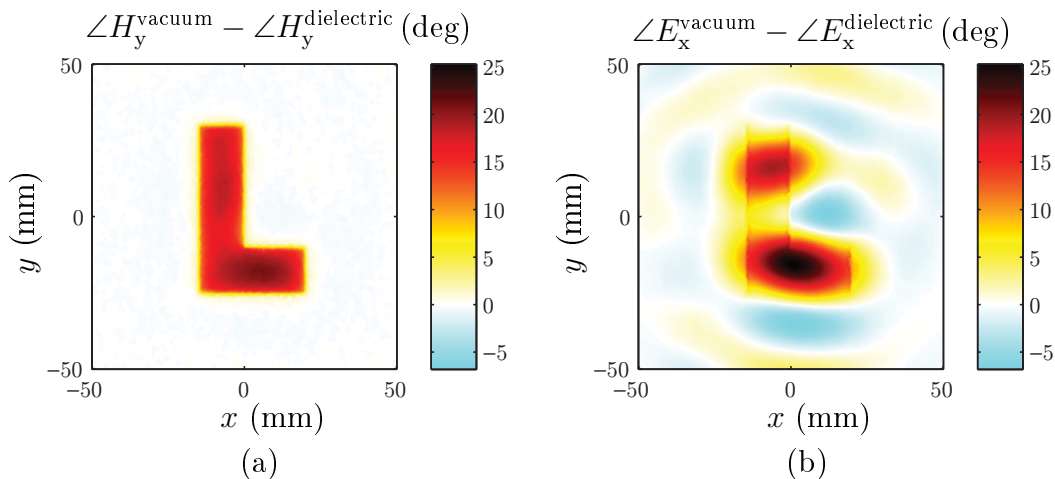
Figure 6: The phase differences simulated in CST. The incoming electric field is polarized in the $x-$direction. a) Magnetic component H_y. b) Electric component E_x.

in free space. The dielectric patch is $0.9\,\mathrm{mm}$ thick and has an relative permittivity of 4.32. The surrounding box of vacuum has the dimensions $100 \times 100 \times 60\,\mathrm{mm}^3$. In Figure 6, the field differences are visualized $0.02\,\mathrm{mm}$ above the dielectric, *i.e.*, $z = 0.92\,\mathrm{mm}$. The phase of the magnetic component H_y gives clearly a sharper image of the dielectric than the electric component E_x. Simulations with an electric field polarized in the y-direction give similar results, *i.e.*, E_y is less distinct than H_x.

3   Reconstruction algorithm

To localize the defective areas on the radome, we have utilized a surface integral representation to relate the equivalent surface currents on the radome surface to the measured far field [7, 30]. In addition, an electric surface integral equation is applied to ensure that the sources are located inside the radome [7, 30].

A surface integral representation expresses the electric field in a homogeneous and isotropic region in terms of the tangential electromagnetic fields on the bounding surface. In our case, the bounding surface, S_radome, is a fictitious surface, located just outside the physical radome wall, with smoothly capped top and bottom surfaces to form a closed surface. This fictitious surface is located in free space, but for convenience, it is referred to as the radome surface throughout the paper. Combining the source-free Maxwell equations and vector identities gives a surface integral

representation of the electric field [25, 30]

$$
\iint\limits_{S_{\mathrm{radome}}} \left(-\mathrm{j}k\eta_0\, g(\boldsymbol{r}',\boldsymbol{r})\big[\hat{\boldsymbol{n}}(\boldsymbol{r}')\times \boldsymbol{H}(\boldsymbol{r}')\big] - \frac{\eta_0}{\mathrm{j}k}\, \nabla' g(\boldsymbol{r}',\boldsymbol{r})\Big\{\nabla_S'\cdot\big[\hat{\boldsymbol{n}}(\boldsymbol{r}')\times \boldsymbol{H}(\boldsymbol{r}')\big]\Big\} \right.
$$

$$
\left. -\nabla' g(\boldsymbol{r}',\boldsymbol{r})\times\big[\hat{\boldsymbol{n}}(\boldsymbol{r}')\times \boldsymbol{E}(\boldsymbol{r}')\big] \right)\,\mathrm{d}S' = \begin{cases} \boldsymbol{E}(\boldsymbol{r}) & \boldsymbol{r}\ \text{outside}\ S_{\mathrm{radome}} \\ \boldsymbol{0} & \boldsymbol{r}\ \text{inside}\ S_{\mathrm{radome}} \end{cases}
$$

$$(3.1)$$

for the exterior problem where all the sources are located inside S_{radome}. The used time convention is $\mathrm{e}^{\mathrm{j}\omega t}$, ω is the angular frequency, and η_0 is the intrinsic wave impedance of free space. The surface divergence is denoted $\nabla_S\cdot$ [8], the unit normal $\hat{\boldsymbol{n}}$ points outward, and the scalar free-space Green's function is $g(\boldsymbol{r}',\boldsymbol{r}) = \frac{\mathrm{e}^{-\mathrm{j}k|\boldsymbol{r}-\boldsymbol{r}'|}}{4\pi|\boldsymbol{r}-\boldsymbol{r}'|}$, where the wave number is $k=\omega/\mathrm{c}_0$ and c_0 is the speed of light in free space. The representation (3.1) states that if the electromagnetic field on a bounding surface is known, the electromagnetic field in the volume, outside of S_{radome}, can be determined [30]. If these integrals are evaluated at a point $\boldsymbol{r}$ lying in the volume enclosed by S_{radome}, these integrals cancel each other (extinction).

The representation (3.1) consists of three components, two tangential fields and one normal component of the field. Since the normal component can be determined by the knowledge of the tangential parts, this representation contains redundancies. As a consequence, specifying only the tangential components suffice [25]. The measured far field consists of two orthogonal components, $\hat{\boldsymbol{\varphi}}$ (azimuth) and $\hat{\boldsymbol{\theta}}$ (polar). The tangential fields on the radome surface are decomposed into two tangential components along the horizontal, $\hat{\boldsymbol{\varphi}}$, and vertical, $\hat{\boldsymbol{v}}$, arc lengths coordinates, see Figure 1. The lower representation in (3.1) is transformed into a surface integral equation letting $\boldsymbol{r}$ approach S_{radome} from the inside [8, 30]. To simplify, the operators $\mathcal{L}$ and $\mathcal{K}$ are introduced as [17]

$$
\begin{cases} \mathcal{L}(\boldsymbol{X})(\boldsymbol{r}) = \mathrm{j}k \iint\limits_{S_{\mathrm{radome}}} \left\{ g(\boldsymbol{r}',\boldsymbol{r})\boldsymbol{X}(\boldsymbol{r}') - \dfrac{1}{k^2}\, \nabla' g(\boldsymbol{r}',\boldsymbol{r})\big[\nabla_S'\cdot \boldsymbol{X}(\boldsymbol{r}')\big] \right\}\mathrm{d}S' \\[4mm] \mathcal{K}(\boldsymbol{X})(\boldsymbol{r}) = \iint\limits_{S_{\mathrm{radome}}} \nabla' g(\boldsymbol{r}',\boldsymbol{r})\times \boldsymbol{X}(\boldsymbol{r})\,\mathrm{d}S' \end{cases}
$$

$$(3.2)$$

In this notation the surface integral representation and the surface integral equation for the electric field (EFIE) yield

$$
\begin{bmatrix} \hat{\boldsymbol{\theta}}(\boldsymbol{r}) \\ \hat{\boldsymbol{\varphi}}(\boldsymbol{r}) \end{bmatrix} \cdot \Big\{ -\mathcal{L}\,(\eta_0\boldsymbol{J})\,(\boldsymbol{r}) + \mathcal{K}\,(\boldsymbol{M})\,(\boldsymbol{r}) \Big\} = \begin{bmatrix} \hat{\boldsymbol{\theta}}(\boldsymbol{r})\cdot \boldsymbol{E}(\boldsymbol{r}) \\ \hat{\boldsymbol{\varphi}}(\boldsymbol{r})\cdot \boldsymbol{E}(\boldsymbol{r}) \end{bmatrix} \qquad \boldsymbol{r}\in S_{\mathrm{meas}} \qquad (3.3)
$$

$$
\hat{\boldsymbol{n}}(\boldsymbol{r})\times \Big\{ \mathcal{L}\,(\eta_0\boldsymbol{J})\,(\boldsymbol{r}) - \mathcal{K}\,(\boldsymbol{M})\,(\boldsymbol{r}) \Big\} = \frac{1}{2}\,\boldsymbol{M}(\boldsymbol{r}) \qquad \boldsymbol{r}\in S_{\mathrm{radome}} \qquad (3.4)
$$

where S_{meas} is the set of discrete sample points (*cf.*, Figure 3), and S_{radome} is the fictitious surface located precisely outside the physical radome wall with a smoothly

capped top and bottom. In a similar manner, a surface integral equation of the magnetic field (MFIE) can be derived,

$$\hat{\boldsymbol{n}}(\boldsymbol{r}) \times \left\{ \mathcal{L}\left(\boldsymbol{M}\right)(\boldsymbol{r}) + \mathcal{K}\left(\eta_0 \boldsymbol{J}\right)(\boldsymbol{r}) \right\} = -\frac{\eta_0}{2} \boldsymbol{J}(\boldsymbol{r}) \qquad \boldsymbol{r} \in S_{\mathrm{radome}} \qquad (3.5)$$

In (3.3)–(3.5) we have introduced the equivalent surface currents on the radome surface, $\boldsymbol{J} = \hat{\boldsymbol{n}} \times \boldsymbol{H}$ and $\boldsymbol{M} = -\hat{\boldsymbol{n}} \times \boldsymbol{E}$ [17]. As mentioned above, the tangential fields on the radome surface are decomposed into two components along the horizontal and vertical arc lengths coordinates of the surface, that is $[\hat{\boldsymbol{\varphi}}, \hat{\boldsymbol{v}}, \hat{\boldsymbol{n}}]$ forms a right-handed coordinate system. Throughout the paper we use the notations, $H_{\mathrm{v}} = \boldsymbol{H} \cdot \hat{\boldsymbol{v}} = -J_{\varphi}$, $H_{\varphi} = \boldsymbol{H} \cdot \hat{\boldsymbol{\varphi}} = J_{\mathrm{v}}$, $E_{\mathrm{v}} = \boldsymbol{E} \cdot \hat{\boldsymbol{v}} = M_{\varphi}$, and $E_{\varphi} = \boldsymbol{E} \cdot \hat{\boldsymbol{\varphi}} = -M_{\mathrm{v}}$ for the reconstructed tangential electromagnetic fields.

The representation (3.3) can be used together with EFIE (3.4), MFIE (3.5), or a combination of both (CFIE), to avoid internal resonances [5, 7]. We have solved the problem by using both EFIE and MFIE separately together with the representation. The results do not differ significantly from each other. As a consequence, there are no problems with internal resonances for the employed set-up and choice of operators, since the internal resonance frequencies of EFIE and MFIE differ [5]. In Section 4, the results using (3.3) together with (3.4) are visualized.

The surface integral equations are written in their weak forms, *i.e.*, they are multiplied with a test function and integrated over their domain [5, 21]. The set-up, see Figure 3, is axially symmetric. Consequently, a Fourier expansion reduces the problem by one dimension [24]. Only the Fourier components of the fields with Fourier index $m = [-40, 40]$ are relevant, since the amplitudes of the field differences of higher modes are below $-60\,\mathrm{dB}$, for all measurement series and configurations. Convergence studies show that this choice is sufficient.

The system of equations in (3.3)–(3.5) is solved by a body of revolution method of moments (MoM) code [2, 24]. The evaluation of the Green's functions is based on [13]. The basis function in the $\hat{\boldsymbol{\varphi}}$-direction consists of a piecewise constant function, and a global function, a Fourier basis, of coordinate φ. Moreover, the basis function in the $\hat{\boldsymbol{v}}$-direction consists of a piecewise linear function, 1D rooftop, of the coordinate v, and the same global function as the basis function in the $\hat{\boldsymbol{\varphi}}$-direction, see Figure 1 for notation. Test functions are chosen according to Galerkin's method [5], and the height (arc length) is uniformly discredited in steps of $\lambda/12$. The surface is described by a second order approximation.The in-house MoM code is verified by scattering of perfect electric conductors (PEC) and dielectric spheres [32].

The problem is regularized by a singular value decomposition (SVD), where the influence of small singular values is reduced [15]. A reference measurement series is performed to set the regularizing parameter used in the subsequent series, see Section 4.1. The inversion of the matrix system is verified using synthetic data. Moreover, the results, which localize the given defects, serve as good verifications.

The described method are applied in [26–28], to reconstruct equivalent surface currents from a measured near field. A slightly different approach is found in [18, 19]. Specifically, the surface integral representation, the EFIE, and the MFIE are solved utilizing higher order bases functions in a MoM solver with a Tikhonov regularization. In [3, 4, 10], the EFIE and MFIE are evaluated on a surface located inside the

surface of reconstruction, and the matrix system is solved by an iterative conjugate-gradient solver. Yet another approach is given in [1, 22, 23], where a surface integral representation is employed together with a conjugate-gradient solver as well as a singular value decomposition. In [9] the authors make use of dyadic Green's functions.

4   Reconstruction results

Three different configurations are investigated at $10\,\mathrm{GHz}$; (0) antenna, (1) antenna together with the radome, and (2) antenna together with the radome where patches of metal or dielectric material are attached to the surface, see Figure 1. The field is measured in the far-field region, as described in Section 2.1. The equivalent surface currents, both amplitude and phase, are reconstructed on a fictitious surface shaped as the radome. Observe, even in the case when only the antenna is present — conf. (0) — the field is reconstructed on a radome shaped surface.

The magnetic component, H_v, is analyzed in this section, since it gives the sharpest image of the phase shifts (*cf.*, the discussion in Section 2.2). Moreover, the components H_φ and E_v are small cross-polarization terms, and a pronounced influence of the phase shift due to a thin dielectric patch of tape are not visible in these components. For this reason, these components are not investigated. The notation used in visualizing the phase difference between the fields from *e.g.*, conf. (1) and (2), is $\angle H_\mathrm{v}^{(1)} - \angle H_\mathrm{v}^{(2)} = \frac{180}{\pi} \angle \left\{ H_\mathrm{v}^{(1)} [H_\mathrm{v}^{(2)}]^* \right\}$, where the star denotes the complex conjugate. The employed time convention, $\mathrm{e}^{\mathrm{j}\omega t}$, gives a negative phase shift, indicating that $\angle H_\mathrm{v}^{(1)} - \angle H_\mathrm{v}^{(2)} > 0°$.

4.1   Reference measurement

First, a measurement series is conducted where copper plates are attached to the radome surface in conf. (2). The imaging results agree well with the ones presented in [26–28], where near-field measurements are utilized, and these results are not further investigated in this paper. However, this first measurement series acts as a reference measurement and sets the regularization parameter of the SVD used in the subsequent measurement series. Typical graphs of the singular values are shown in Figure 7. Each curve shows the singular value for the operator with Fourier index m, normalized to the largest singular value ($i = 1$) for $m = 0$. As $|m|$ increases, the "knee" of the graph, where the singular values start to rapidly decrease, appears more quickly. The regularization parameter is chosen where the "knee" bends. Investigations have shown that the chosen value is robust for a given set-up and frequency. Furthermore, the results are not significantly altered if a slightly different value is employed. The interval Δ in Figure 7 indicates where the regularization parameter gives a reliable outcome. The regularization parameter is set to $-29.8\,\mathrm{dB}$, and this parameter is then utilized in the processing of the succeeding measurement series.
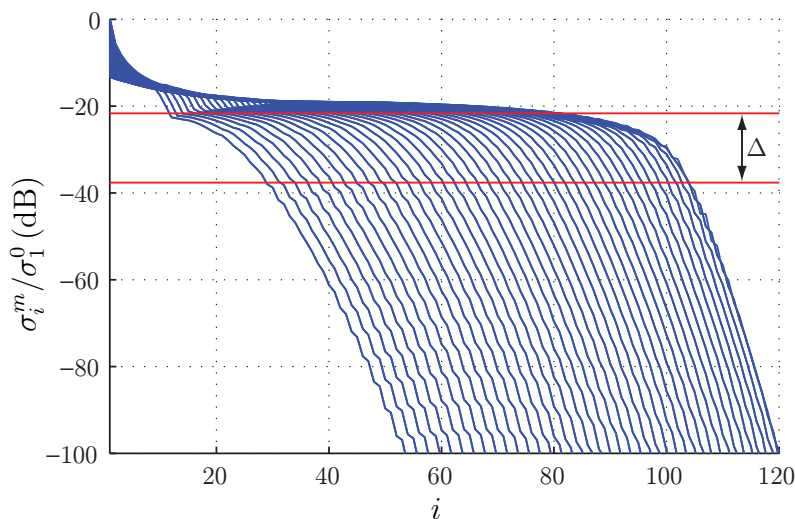
Figure 7: Singular values σ_i^m. Each curve depicts different Fourier index m, and the curves are normalized to the largest singular value for $m = 0$. The interval, Δ, where the regularization parameter gives a reliable outcome, is drawn.

4.2 Imaging of dielectric material

Obtaining a constant phase shift over the illuminated area is often important to trim radomes. The trimming is achieved by adding or removing dielectric material to the radome surface. To investigate if the proposed method can be utilized to map areas of the radome surface with a deviating electrical thickness, patches of dielectric material (defects), are attached to the radome surface in conf. (2). Defects of dielectric material mainly affect the phase of the field, and the phase differences of the fields for the different configurations give us an understanding of how the defects delay the fields.

Measurement series number two and three are employed. In each series the field from the antenna (conf. (0)), the antenna together with the radome (conf. (1)), and the antenna together with the radome where dielectric patches are attached to the surface (conf. (2)), were measured, *cf.*, Figure 1. In the second measurement series, squares are added to the area where the main lobe illuminates the radome, see Figure 8a, where the size and the thickness of the patches are shown. In the third measurement series, the letters LU are attached to the radome, see Figure 8b.

4.2.1 Dielectric squares

Eleven dielectric squares of the sizes 0.5λ, 1λ, and 2λ are added to the radome surface, see Figures 8a and 9. In Figure 9b, the illumination of the area of conf. (1), to which the dielectric squares will be applied to create one case of conf. (2), is shown. The largest squares are located in a field region of $[-23, -6]$ dB, the middle sized in the region $[-12, 0.3]$ dB and the smallest ones in $[-9, 0.3]$ dB, respectively. In Figures 9c and 10, the reconstructed phase shifts due to the defects, $\angle H_v^{(1)} - \angle H_v^{(2)}$, are visualized. The squares of size 2λ are clearly visible even though they are partly
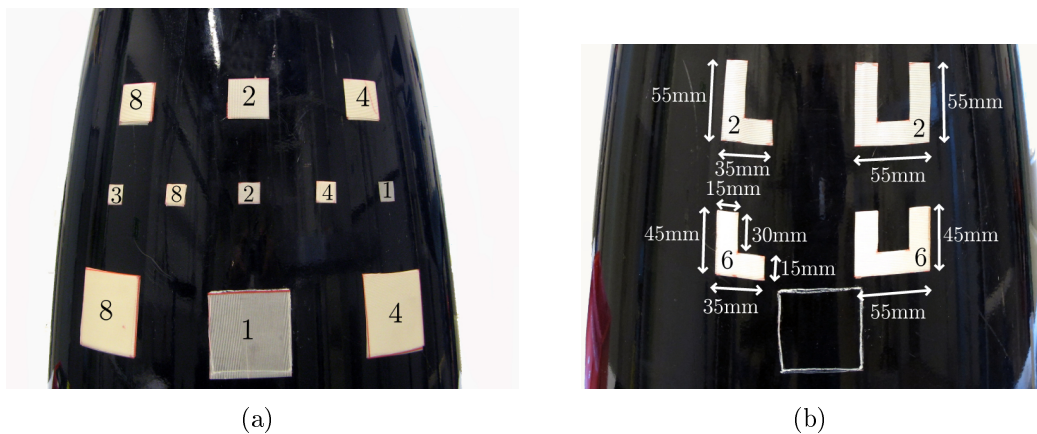
(a) (b)

Figure 8: The dielectric defects attached to the radome in conf. (2) — measurement series number two and three, respectively. The numbers on the patches indicate the number of tape layers. a) The size of the squares are; $30 \times 30\,\text{mm}^2$ on the top row, $15 \times 15\,\text{mm}^2$ on the middle row, and $60 \times 60\,\text{mm}^2$ on the bottom row. b) Each "leg" has a width of $15\,\text{mm}$. The drawn square indicates where the centered lower square in the left figure was located.

located in areas with lower illumination. The ones of size 1λ are also easily found. The defects of size 0.5λ with thickness of four and eight layers are also clearly visible, even though the phase shift is not as conspicuous here. The thinner, small squares tend to blend into the background phase deviation, but since we know where to look, even these can be identified. The rounded corners are due to the limited resolution. According to (2.2), each layer gives rise to a phase shift of approximately $2° - 3°$. To get an estimate of the phase shift due to the added squares, an average value is calculated over the areas indicated in Figure 9b. These areas are drawn according to the given coordinates of the squares, *i.e.*, their positions are not approximated from the reconstruction. The average values of the phase shifts are given in Table 1 and they agree very well for the larger squares.

	1 layer	2 layers	3 layers	4 layers	8 layers
0.5λ	2°	3°	4°	5°	10°
1λ		6°		12°	22°
2λ	2°			10°	19°
Phase shift due to (2.2)	$2° - 3°$	$4° - 6°$	$6° - 9°$	$8° - 12°$	$16° - 24°$

Table 1: The average phase shift due to the dielectric squares. The bottom row gives an approximate theoretical calculation, based on (2.2).
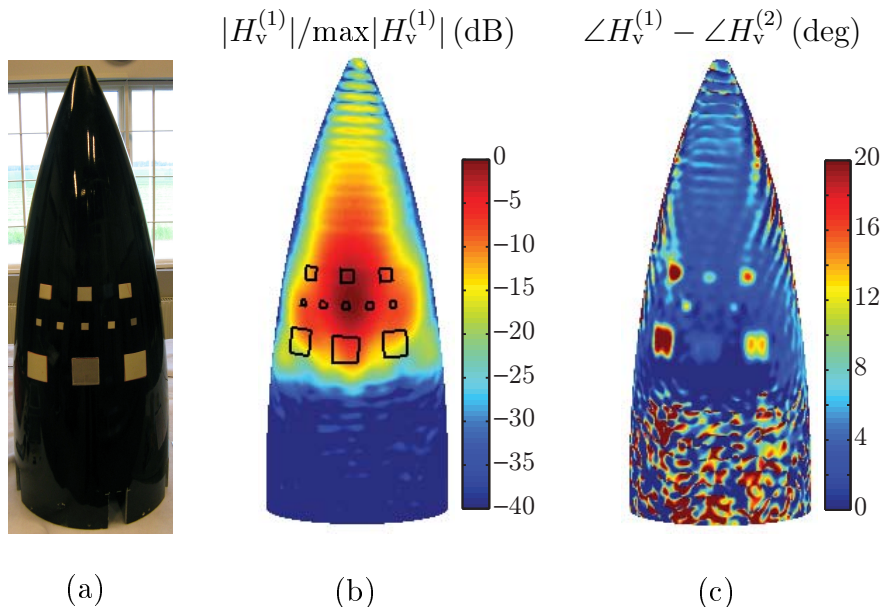
$$|H_{\rm v}^{(1)}|/\max|H_{\rm v}^{(1)}| \, ({\rm dB}) \qquad \angle H_{\rm v}^{(1)} - \angle H_{\rm v}^{(2)} \, ({\rm deg})$$

(a)   (b)   (c)

Figure 9: a) A photo of the radome with the dielectric squares (defects). b) The reconstructed field, $H_{\rm v}$, on the radome — conf. (1). The drawn squares indicate where the defects will be located to create conf. (2). c) The phase of the reconstructed field difference between conf. (1) and (2).

4.2.2   Dielectric letters LU

In the third measurement series, defects of dielectric tape in the form of the letters LU, are investigated, see Figures 8b and 11. The thickness of the tape is six layers for the lower LU and two layers for the top one. The illumination of the area of conf. (1), to which the dielectric letters will be applied to create one case of conf. (2), is shown in Figure 11b. The ranges of the field within the defects are, from the top left to the bottom right; $[-8, -4]\,{\rm dB}$, $[-5, 0.3]\,{\rm dB}$, $[-8, -6]\,{\rm dB}$, and $[-9, -1]\,{\rm dB}$, respectively. In Figures 11c and 12a, the reconstructed phase shifts due to the defects, $\angle H_{\rm v}^{(1)} - \angle H_{\rm v}^{(2)}$, are visualized. All letters are clearly visible in the reconstruction. As stated above, each layer of tape shifts the phase by approximately $2° - 3°$. This agrees very well with the results given in Figure 12b, where the line plots reveal how the phase difference changes due to the dielectric letters. The defects on the bottom have a maximum deviation of about $16°$ and the top ones circa $6°$.

4.2.3   Differences with the antenna as a reference

In the previous sections, we have looked at phase differences between the radome with attached defects and the radome itself, *i.e.*, the differences between conf. (1) and (2). This has given an estimate of how well phase objects can be reconstructed. In practice, it is advantageous to visualize the influence of the non-optimized radome. In our measurements, this corresponds to the difference between conf. (0) and conf. (1) or (2). The reconstructed phase shift over the illuminated area can act as a trimming mask, indicating areas where a thickness alteration is required, in
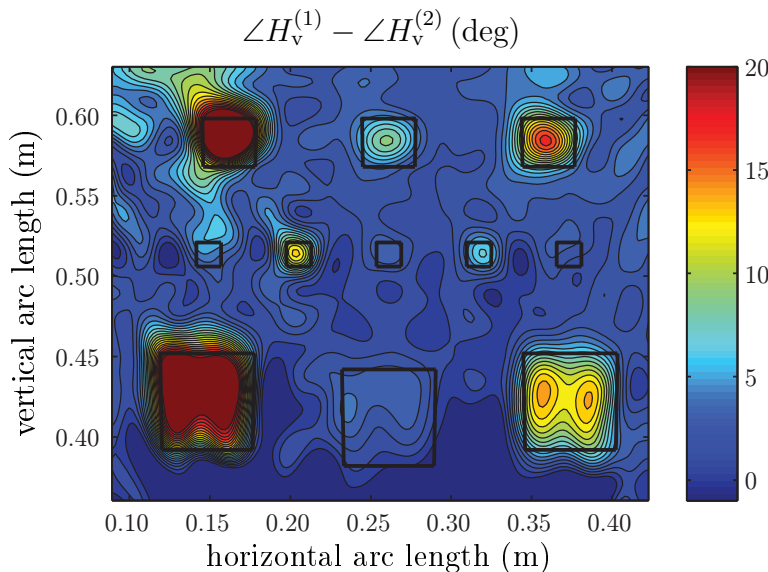
Figure 10: Enlarged view of the area with the dielectric squares in Figure 9c. The phase of the reconstructed field difference between conf. (1) and (2) is depicted. Each contour line represents one degree. The drawn squares indicate the given coordinates, *i.e.*, their positions are not approximated from the reconstruction.

order to get the phase shift into a pre-defined interval.

The influence of the radome in the main lobe, $\angle H_{\mathrm{v}}^{(0)} - \angle H_{\mathrm{v}}^{(1)}$, is visualized for the second measurement series in Figure 13a. The same difference $(\angle H_{\mathrm{v}}^{(0)} - \angle H_{\mathrm{v}}^{(1)})$ is shown in Figure 14a for the third measurement series, and it becomes clear that there is a small deviation between the conf. (0) and (1) between measurement series. Instead of a desired constant phase shift in the main lobe, Figures 13a and 14a indicate a phase shift of $115° \pm 10°$, implying that the radome surface needs to be trimmed. The drawn squares and letters, in the figures, point out where the defects are to be located to create conf. (2).

In Figures 13b and 14b, the phase difference in the main lobe between conf. (0) and conf. (2) $(\angle H_{\mathrm{v}}^{(0)} - \angle H_{\mathrm{v}}^{(2)})$ is shown for the dielectric squares and letters LU. The phase shift introduced by the dielectric patches in conf. (2) is now added to the phase shift caused by the radome itself. The upper squares in Figure 13b are mainly located in areas where the phase shift due to the radome itself is already large, therefore these squares are clearly seen. The lower ones, to the left and right, are thick enough to give rise to a visible phase shift by themselves. The square in the middle on the bottom row is only one layer thick and located in a region with a low phase shift to start with, and it cannot be resolved in the dynamic range showed. Most parts of the letters LU are seen in the reconstructed images, see Figure 14b. However, the left "legs" of the U:s are not as visible. The reason is that these parts are attached to an area, where an added patch (with the appropriate thickness) increases the phase shift to the level of the surrounding areas, and it is thereby not localized by itself.
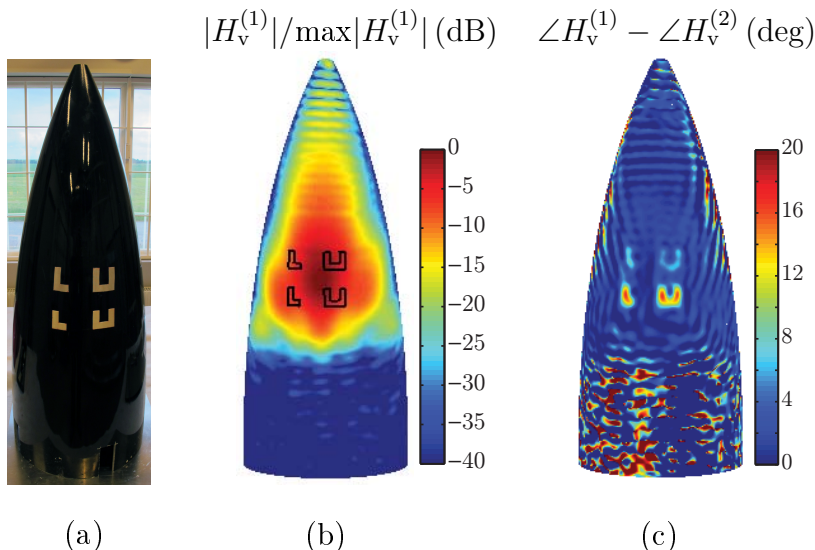
$|H_v^{(1)}|/\max|H_v^{(1)}|$ (dB) $\angle H_v^{(1)} - \angle H_v^{(2)}$ (deg)

(a)   (b)   (c)

Figure 11: a) A photo of the radome with the attached dielectric letters LU (defects). b) The reconstructed field, H_v, on the radome — conf. (1). The drawn lines indicate where the letters will be located to create conf. (2). c) The phase of the reconstructed field difference between conf. (1) and (2).

4.2.4   Trimband

A horizontal band in the phase images is discovered during the investigations, see Figure 15. Visual inspection reveals a small indentation on the inside of the radome wall, originating from an earlier attempt to trim the radome. The indentation starts at the approximate height 0.6 m (arc length) with a width of 0.1 m. In Figure 15a, the reconstructed field from the antenna (conf. (0)), projected on the radome surface, is shown, to visualize the illumination. The black lines indicate where the band is located. The phase deviation between the band and the surrounding areas is approximately −15° to −10°, see Figure 15b.

To verify the phase deviation, the phase deviation is related to a wall thickness by employing the approximate formula in (2.2). The utilized material parameters are $\epsilon_r \approx 4.32$ and $\tan\delta \approx 0.0144$ (*cf.*, Section 2.1). Estimating the angle of incidence to 60°, see Figure 3, results in a wall thickness of $0.6 - 0.9$ mm. This approximated value agrees well with the actual indentation on the radome. The phase differences, at the top and the bottom of the radome in Figure 15b are not reliable due to low illumination.

5   Conclusions and discussions

Techniques to diagnose radomes are requested in *e.g.*, performance verifications. In [26–28], the influence of copper plates, *e.g.*, amplitude reduction and appearance of flash (image) lobes, are investigated together with the localization of the defect areas on the radome surface. In this paper, we investigate how reconstructed equivalent surface currents from a measured far field can assist in localizing phase defects on a radome. The phase defects introduce a hardly noticeable change in the far-field
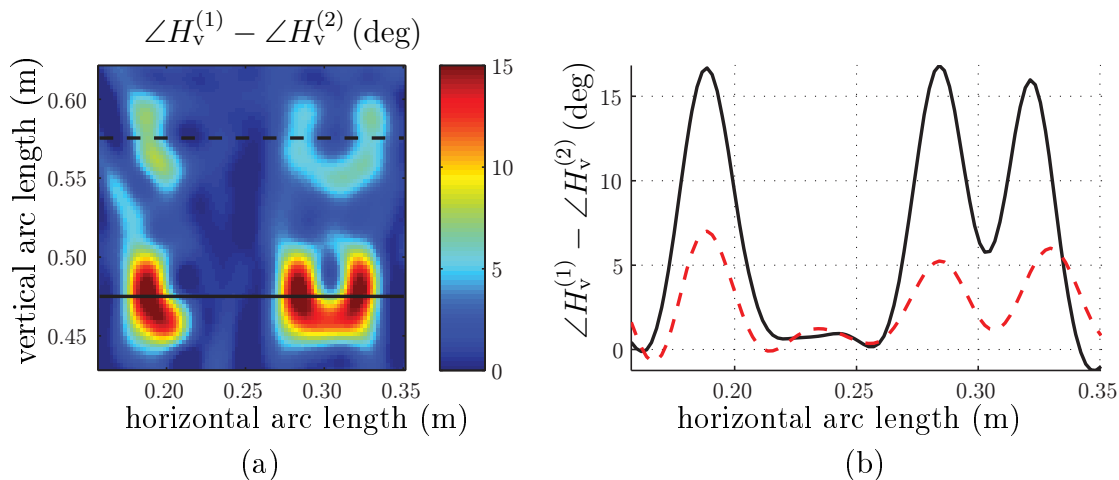
Figure 12: a) Enlarged view of the area with the dielectric letters in Figure 11c. The phase of the reconstructed field difference between conf. (1) and (2) is depicted. b) Line plot through the letters showing the phase deviations. The solid line in the left image corresponds to the solid line in the right plot *etc.*

pattern. However, by visualizing the insertion phase delay (IPD) in the illuminated area of the radome, the locations of the defects are revealed.

Dielectric squares of size 2λ — one layer thick, squares of size 1λ — two layer thick, and squares of size 0.5λ — 4 layer thick, are clearly visible in the reconstructed phase differences. One layer tape corresponds to a phase shift of a couple degrees. Furthermore, the dielectric tapes of two layers and the smallest dimension of 0.5λ in the form of the letters LU are resolved. The phase shifts of the larger squares and the letters coincide well with the approximated theoretical ones. The radiance at the upper left corner of the lower dielectric L, see *e.g.*, Figure 12a, needs to be investigated further. Possible explanations might be constructive and destructive interference due to edge effects, noise influence, or a combination thereof. Analyzes of other field components might explain this phenomenon. Future studies will address the questions of how to combine the components to increase the resolution.

Reconstructing the fields on the radome surface, the magnetic field gives sharper images than the electric field. A qualified explanation is that the induced currents on the attached patches are of electric nature. This effect is also verified by simulations in CST Microwave Studio.

The results indicate that the diagnostic method, beyond what is proposed in [26–28], can be used in constructing a trimming mask for the illuminated areas of a radome. The mask gives instructions of how to alter the radome surface, in order to change the IPD, side and flash (image) lobes, to their preferable values. To indicate how this can be implemented, we have explored the phase influence of the radome itself, and then the radome with attached patches of dielectric tape. Even if the main purpose of this paper is not to suggest how to trim the radome, we observe that adding dielectric patches gives a smoother phase shift in areas where the phase shift due to the radome itself is smaller than in the surrounding areas. In an upcoming paper, these images and their potential to alter the IPD and flash (image) lobes will be addressed.
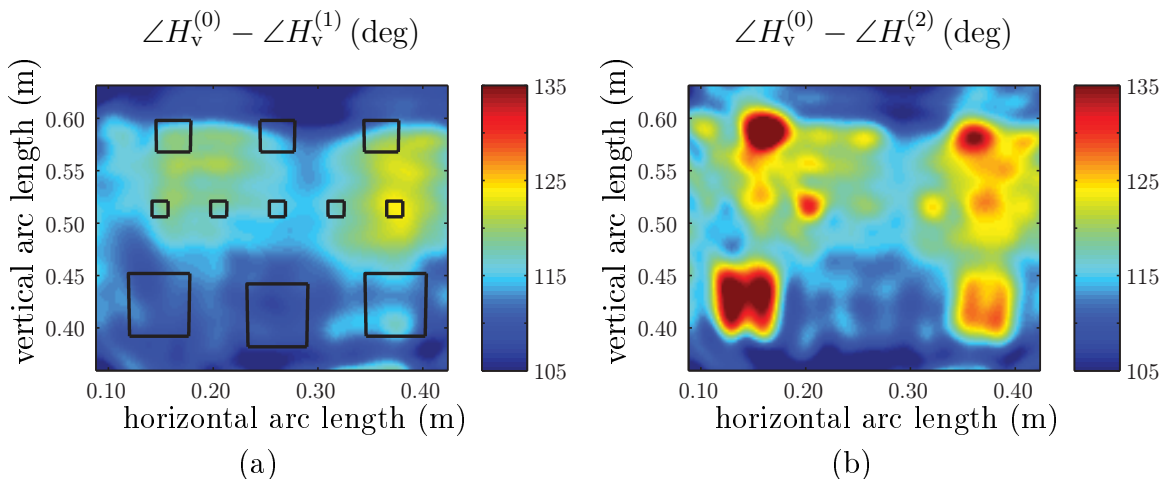
Figure 13: Enlarged view of the area illuminated by the main lobe. Phase differences reconstructed from measurement series number two. a) Phase changes due to the radome. The drawn squares indicate where the dielectric patches will be located to create conf. (2). b) Phase changes due to the radome together with the dielectric squares.

Acknowledgement

Appendix A   Induced currents due to dielectrics

A dielectric material introduces induced currents in the Maxwell equations. To see this, start with the Maxwell equations for time harmonic fields in a source free region (time convention $e^{j\omega t}$),

$$\nabla \times \boldsymbol{E} = -j\omega \boldsymbol{B}$$
$$\nabla \times \boldsymbol{H} = j\omega \boldsymbol{D}$$

where $\boldsymbol{E}$ is the electric field, $\boldsymbol{B}$ is the magnetic flux density, $\boldsymbol{H}$ is the magnetic field, and $\boldsymbol{D}$ is the electric flux density, respectively.   The constitutive relations read $\boldsymbol{D} = \epsilon_0 \epsilon_r \boldsymbol{E}$ and $\boldsymbol{B} = \mu_0 \mu_r \boldsymbol{H}$, where ϵ_0 is the permittivity of free space, ϵ_r is the relative permittivity, μ_0 is the permeability of free space, and μ_r is the relative permeability, respectively.

In the absence of defects, and outside the radome (conf. (1) in Figure 1) we have

$$\nabla \times \boldsymbol{E}^{(1)} = -j\mu_0\omega \boldsymbol{H}^{(1)}$$
$$\nabla \times \boldsymbol{H}^{(1)} = j\epsilon_0\omega \boldsymbol{E}^{(1)}$$
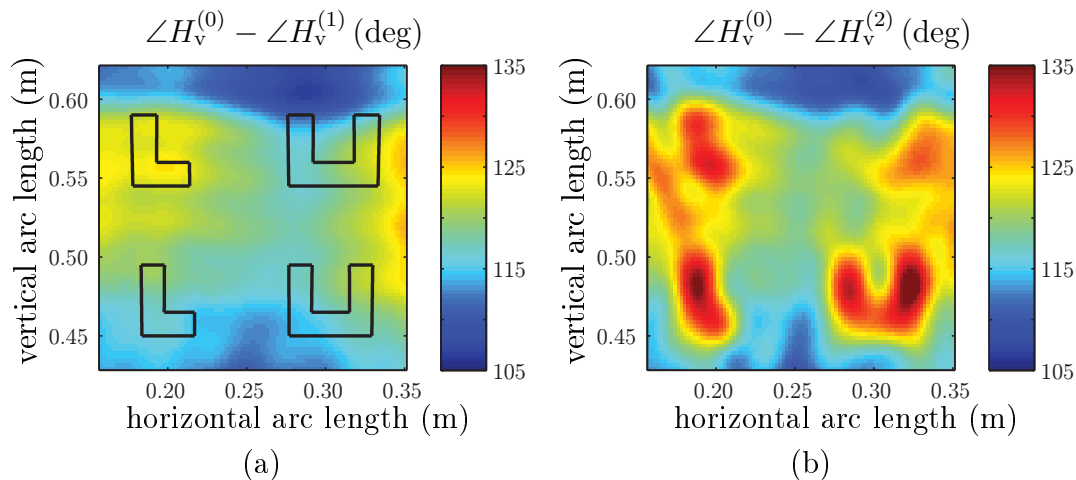
Figure 14: Enlarged view of the area illuminated by the main lobe. Phase differences reconstructed from measurement series number three. a) Phase changes due to the radome. The drawn lines indicate where the dielectric letters will be located to create conf. (2). b) Phase changes due to the radome together with the dielectric letters.

On the other hand, in the presence of a dielectric material (conf. (2)) the defects have an electric susceptibility $\chi_e = \epsilon_r - 1$, giving [16]

$$\begin{aligned}
\nabla \times \boldsymbol{E}^{(2)} &= -j\mu_0\omega\boldsymbol{H}^{(2)} \\
\nabla \times \boldsymbol{H}^{(2)} &= j\epsilon_0\omega\boldsymbol{E}^{(2)} + j\epsilon_0\chi_e\omega\boldsymbol{E}^{(2)}
\end{aligned}$$

The field differences $\boldsymbol{E} = \boldsymbol{E}^{(2)} - \boldsymbol{E}^{(1)}$ and $\boldsymbol{H} = \boldsymbol{H}^{(2)} - \boldsymbol{H}^{(1)}$ satisfy

$$\begin{aligned}
\nabla \times \boldsymbol{E} &= -j\mu_0\omega\boldsymbol{H} \\
\nabla \times \boldsymbol{H} &= j\epsilon_0\omega\boldsymbol{E} + \boldsymbol{J}_{\chi_e}
\end{aligned}$$

where $\boldsymbol{J}_{\chi_e} = j\epsilon_0\chi_e\omega\boldsymbol{E}^{(2)}$ is interpreted as the induced current.

References

[1] Y. Alvarez, F. Las-Heras, and C. Garciain. The sources reconstruction method for antenna diagnostics and imaging applications. In A. Kishk, editor, *Solutions and Applications of Scattering, Propagation, Radiation and Emission of Electromagnetic Waves*. InTech, 2012.

[2] M. Andreasen. Scattering from bodies of revolution. *IEEE Trans. Antennas Propagat.*, **13**(2), 303–310, 1965.

[3] J. L. A. Araque Quijano, L. Scialacqua, J. Zackrisson, L. J. Foged, M. Sabbadini, and G. Vecchi. Suppression of undesired radiated fields based on equivalent currents reconstruction from measured data. *Antennas and Wireless Propagation Letters, IEEE*, **10**, 314–317, 2011.
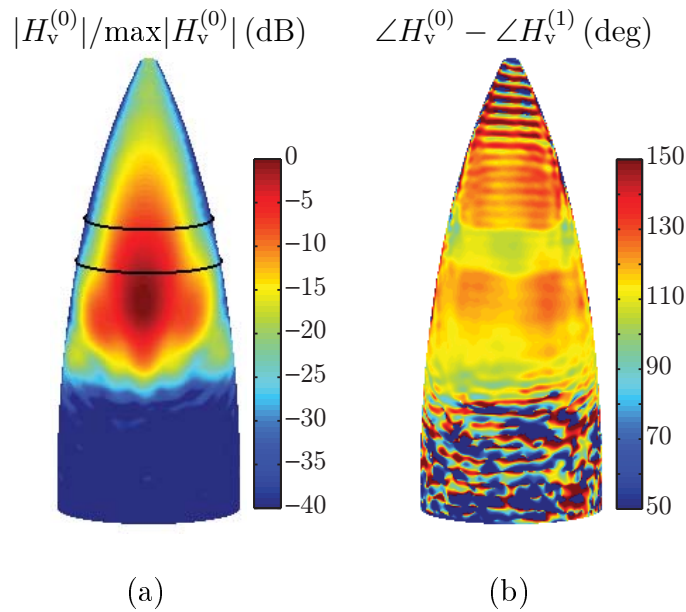
$|H_{\mathrm{v}}^{(0)}|/\max|H_{\mathrm{v}}^{(0)}|$ (dB) $\angle H_{\mathrm{v}}^{(0)} - \angle H_{\mathrm{v}}^{(1)}$ (deg)

(a)   (b)

Figure 15: Phase image of an earlier attempt to trim the radome. a) The illumination of the radome. The black lines indicate the location of the indentation. b) Phase change due to the radome.

[4] J. L. A. Araque Quijano and G. Vecchi. Field and source equivalence in source reconstruction on 3D surfaces. *Progress In Electromagnetics Research*, **103**, 67–100, 2010.

[5] A. Bondeson, T. Rylander, and P. Ingelström. *Computational Electromagnetics*. Springer-Verlag, Berlin, 2005.

[6] D. G. Burks. Radomes. In J. L. Volakis, editor, *Antenna engineering handbook*. pub-mcgraw, fourth edition, 2007.

[7] W. C. Chew, M. S. Tong, and B. Hu. *Integral equation methods for electromagnetic and elastic waves*, volume 12. Morgan & Claypool, 2008.

[8] D. Colton and R. Kress. *Integral Equation Methods in Scattering Theory*. John Wiley & Sons, New York, 1983.

[9] T. F. Eibert, E. Kaliyaperumal, and C. H. Schmidt. Inverse equivalent surface current method with hierarchical higher order basis functions, full probe correction and multilevel fast multipole acceleration. *Progress In Electromagnetics Research*, **106**, 377–394, 2010.

[10] L. J. Foged, L. Scialacqua, F. Saccardi, J. L. Araque Quijano, G. Vecchi, and M. Sabbadini. Practical application of the equivalent source method as an antenna diagnostics tool. *IEEE Antennas and Propagation Magazine*, **54**(5), 243–249, 2012.

[11] E. Gimonet, A. Sarremejean, J. P. David, and P. Bossuet. Determination of radome pertubation by inverse transform of radiation pattern. In *Proc. of 5th*

European Electromagnetic Windows Conference, pages 183–190, Juan-les-Pins, France, 1989.

[12] M. G. Guler and E. B. Joy. High resolution spherical microwave holography. *IEEE Trans. Antennas Propagat.*, **43**(5), 464–472, 1995.

[13] M. Gustafsson. Accurate and efficient evaluation of modal Green's functions. *Journal of Electromagnetic Waves and Applications*, **24**(10), 1291–1301, 2010.

[14] J. E. Hansen, editor. *Spherical Near-Field Antenna Measurements.* Number 26 in IEE electromagnetic waves series. Peter Peregrinus Ltd., Stevenage, UK, 1988. ISBN: 0-86341-110-X.

[15] P. C. Hansen. *Discrete inverse problems: insight and algorithms*, volume 7. Society for Industrial & Applied, 2010.

[16] J. D. Jackson. *Classical Electrodynamics.* John Wiley & Sons, New York, third edition, 1999.

[17] J. M. Jin. *Theory and computation of electromagnetic fields.* Wiley Online Library, 2010.

[18] E. Jörgensen, D. W. Hess, P. Meincke, O. Borries, C. Cappellin, and J. Fordham. Antenna diagnostics on planar arrays using a 3D source reconstruction technique and spherical near-field measurements. In *Antennas and Propagation (EUCAP), Proceedings of the 6th European Conference on*, pages 2547–2550. IEEE, 2012.

[19] E. Jörgensen, P. Meincke, and C. Cappellin. Advanced processing of measured fields using field reconstruction techniques. In *Antennas and Propagation (EUCAP), Proceedings of the 5th European Conference on*, pages 3880–3884. IEEE, 2011.

[20] D. J. Kozakoff. *Analysis of Radome-Enclosed Antennas.* Artech House, Boston, London, 1997.

[21] R. Kress. *Linear Integral Equations.* Springer-Verlag, Berlin Heidelberg, second edition, 1999.

[22] Y. A. Lopez, F. Las-Heras Andres, M. R. Pino, and T. K. Sarkar. An improved super-resolution source reconstruction method. *Instrumentation and Measurement, IEEE Transactions on*, **58**(11), 3855–3866, 2009.

[23] J. A. Lopez-Fernandez, M. Lopez-Portugues, Y. Alvarez Lopez, C. G. Gonzalez, D. Martínez, and F. Las-Heras. Fast antenna characterization using the sources reconstruction method on graphics processors. *Progress In Electromagnetics Research*, **126**, 185–201, 2012.

[24] J. R. Mautz and R. F. Harrington. Radiation and scattering from bodies of revolution. *Appl. Scientific Research*, **20**(1), 405–435, 1969.

[25] C. Müller. *Foundations of the Mathematical Theory of Electromagnetic Waves.* Springer-Verlag, Berlin, 1969.

[26] K. Persson, M. Gustafsson, and G. Kristensson. Reconstruction and visualization of equivalent currents on a radome using an integral representation formulation. *Progress In Electromagnetics Research*, **20**, 65–90, 2010.

[27] K. Persson and M. Gustafsson. Reconstruction of equivalent currents using a near-field data transformation – with radome applications. *Progress in Electromagnetics Research*, **54**, 179–198, 2005.

[28] K. Persson and M. Gustafsson. Reconstruction of equivalent currents using the scalar surface integral representation. Technical Report LUTEDX/(TEAT-7131)/1–25/(2005), Lund University, Department of Electrical and Information Technology, P.O. Box 118, S-221 00 Lund, Sweden, 2005. http://www.eit.lth.se.

[29] Z. Shengfang, G. Dongming, K. Renke, J. Zhenyuan, S. Aifeng, and J. Tian. Research on microwave and millimeter-wave IPD measurement system for radome. In *Microwave and Millimeter Wave Technology, 2004. ICMMT 4th International Conference on, Proceedings*, pages 711–714. IEEE, 2004.

[30] S. Ström. Introduction to integral representations and integral equations for time-harmonic acoustic, electromagnetic and elastodynamic wave fields. In V. V. Varadan, A. Lakhtakia, and V. K. Varadan, editors, *Field Representations and Introduction to Scattering*, volume 1 of *Handbook on Acoustic, Electromagnetic and Elastic Wave Scattering*, chapter 2, pages 37–141. Elsevier Science Publishers, Amsterdam, 1991.

[31] A. B. Strong. *Fundamentals of composites manufacturing: materials, methods and applications.* Society of Manufacturing Engineers, 2008.

[32] J. G. Van Bladel. *Electromagnetic Fields.* IEEE Press, Piscataway, NJ, second edition, 2007.

[33] B. Widenberg. Advanced compact test range for both radome and antenna measurement. In *11th European Electromagnetic Structures Conference*, pages 183–186, Torino, Italy, 2005.

[34] A. D. Yaghjian. An overview of near-field antenna measurements. *IEEE Trans. Antennas Propagat.*, **34**(1), 30–45, January 1986.